14

Unriddling the role of alkali metal cations and Pt-surface hydroxide in

15 alkaline hydrogen evolution reaction

- 16 Aamir Hassan Shah¹, Zisheng Zhang¹, Zhihong Huang², Sibo Wang¹, Guangyan Zhong¹,
- 17 Chengzhang Wan^{1,2}, Anastassia N. Alexandrova^{1*}, Yu Huang^{2,3*}, Xiangfeng Duan^{1,3,*}
- ¹Department of Chemistry and Biochemistry, University of California, Los Angeles; California
- 19 90095, United States.
- ²Department of Materials Science and Engineering, University of California, Los Angeles;
- 21 California 90095, United States.
- ³California NanoSystems Institute, University of California, Los Angeles; California 90095,
- 23 United States.
- *Correspondence: xduan@chem.ucla.edu, yhuang@seas.ucla.edu, ana@chem.ucla.edu
- 25 The platinum-catalyzed hydrogen evolution reaction (HER) generally shows poorer kinetics
- in alkaline electrolyte and represents a key challenge for alkaline water electrolysis. With the
- 27 presence of alkali metal cations and hydroxyl anions, the electrode-electrolyte (Pt-water)
- interface in alkaline electrolyte is far more complex than that in acidic environment. Herein,
- 29 we combine electrochemical impedance spectroscopy (EIS) and electrical transport
- 30 spectroscopy (ETS) approach to probe and understand the fundamental role of different
- cations (Li⁺, Na⁺ and K⁺) in HER kinetics. Our integrated studies suggest that the alkali
- metal cations play an indirect role in modifying HER kinetics: with the smaller cations less
- destabilizing OH_{ad} in the HER potential window to favor a higher OH_{ad} coverage on Pt
- surface. The surface OH_{ad} is highly polar and acts as both electronically favored proton-
- 35 acceptors and geometrically favored proton-donors to promote water dissociation in alkaline
- media, thus boosting the Volmer step kinetics and the HER activity.
- The hydrogen evolution reaction (HER) is one of the most fundamental and critical reactions in
- 38 renewable energy conversion and storage devices including electrolyzers that convert and store
- intermittent renewable electricity in chemical form by producing hydrogen. On the other hand,
- 40 hydrogen oxidation reaction (HOR) plays a critical role in fuel cell technologies that converts
- 41 stored chemical energy back to electricity. The HER/HOR mechanism and kinetics are drastically

different in acidic and alkaline media^{1,2}. Platinum (Pt) is state of the art electrocatalyst for these reactions and thus significant efforts have been invested in understanding the reaction mechanism and kinetics on Pt-based electrocatalytic systems³⁻⁵. Hitherto, various hypotheses have been proposed to identify and understand the reaction descriptors that account for the pH effect on HER on Pt electrode surfaces. It has been well-recognized that the HER rate and mechanism is related to the strength of metal hydrogen binding energy (HBE). For example, on the basis of a density functional theory (DFT) calculations database of hydrogen chemisorption energies, Nørskov et al. introduced the so-called volcano plot, and confirmed that Pt represents an optimum HER catalyst particularly in acidic environment⁴.

Although the HBE of pure metal surface can in principle serve as an effective physical descriptor for HER, the experimental determination of the relevant physical parameters is often complicated by the presence of the electrolyte and different surface adsorbates, particularly in alkaline electrolytes where the adsorbates are more complex. For example, Yan et al. studied the HER in different pH-buffered electrolytes and suggested that monotonic decrease in HER activities by increasing the pH can be correlated with the continuously strengthened electrochemical HBE values⁶. On the other hand, Koper and coworkers suggested that positive shift in the hydrogen underpotential deposition (H_{upd}) peak in cyclic voltammetry is not because of the HBE changes, but originates from destabilization of the hydroxyl adsorbates (OHad) on Pt(100) and Pt(110) sites by the presence of alkali metal cations near the interface^{7,8}. Moreover, Koper et al. have also shown that the HBE descriptor cannot fully explain the pH dependent catalytic behavior on Pt(111) that shows significant pH dependent HER kinetics yet little pH dependent H_{upd} peak potential shift⁹. Thus, despite the undeniable success of the HBE in acidic media, it is not an unambiguous descriptor for HER/HOR kinetics in alkaline media, largely due to more complex electrolyte environment and the elusive role of different surface adsorbates that may modify the interfacial molecular structures and reaction pathways.

Markovic et al. ascribed the slower HER kinetics in alkaline media to the high energy barrier for H₂O dissociation as compared to the H₃O⁺ in acidic media¹⁰⁻¹², and suggested that the HER kinetics in alkaline media can be improved by presence of oxophilic groups that can stabilize OH_{ad}, which in turn facilitates H₂O dissociation¹³. Later, the same group observed a monotonic relationship between HER activity and the OH_{ad} affinity of the oxophilic groups and concluded that the HER activity follows Brønsted–Evans–Polanyi principle to promote the HER kinetics and

proposed a bifunctional mechanism—the edges of oxophilic metal clusters (M(OH)₂) promote the H₂O dissociation and production of H_{ad} on nearby Pt surfaces that then recombine into molecular hydrogen¹⁴. This bifunctional mechanism has been supported by a number of studies¹⁵⁻¹⁸. For example, Jia and coworkers experimentally verified the bifunctional mechanism by combined electrochemical and operando spectroscopic data¹⁵, and robustly demonstrated that the presence of hydroxyl groups on surface Ru sites in the HOR potential region plays a key role in promoting the rate-determining Volmer step¹⁵. Moreover, Koper et al. recently further investigated the role of OH_{ad} on HER activity in alkaline media and demonstrated that HER activity exhibits a volcanotype relationship with the hydroxide binding strength, supporting Brønsted–Evans–Polyani relationship¹⁹.

Beside HBE and bifunctional mechanism, Koper and coworkers suggested the potential of zero free charge (pzfc) may play an important role⁹. In this picture, the HER/HOR region in acidic media is closer to the pzfc (~0.34 V vs. RHE), and the reorganization energy of interfacial water to move a proton through electrical double layer is small; while the HER/HOR region in alkaline media is far from the pzfc (~1.0 V vs. RHE, i.e. closer to the OH_{ad} region) and the strong electric field in HER/HOR region leads to a large interfacial water reorganization energy that could limit OH⁻ transfers through double layer⁹.

Beside the differences in these distinct theories and different level of success in various aspects, none of them considered the effect of alkali metal cations (AM⁺) on HER kinetics, which can hardly be ignored in alkaline electrolytes. For example, Markovic and coworkers observed promotional HER activity on Ni(OH)₂-Pt surface in the presence of Li⁺ cations and attributed it to water dissociation¹³. Bandarenka and coworkers reported a similar promotion of HER activity on Pt electrode by cations²⁰, and suggested cations may alter the HBE, thus altering the HER activities²⁰. Jia and coworkers attributed the enhancement in HER activity to presence of OH_{ad}-(H₂O)_x-AM⁺ in the double-layer region, which facilitates the removal/transport of OH_{ad} into the bulk, forming OH⁻-(H₂O)_x-AM⁺ as per the hard–soft acid–base theory, thereby promoting HER¹⁶. Koper et al. recently suggested a change in the rate-determining step from Heyrovsky to Volmer step in Li⁺ and K⁺ containing electrolytes, respectively²¹. Overall, although the enhancement of HER activity on Pt electrode in presence of Li⁺ when compared with other larger AM⁺ has been consistently observed, a full understanding of this phenomenon has been a topic considerable

debate. Therefore, to more completely understand the descriptor that dictates HER activity in alkaline media, it is essential to investigate how the different cations alter the local (on-surface or near surface) chemical environment at electrode-electrolyte interface.

Here we address this issue by systematically studying the influence of cations on HER on Pt surface in alkaline media. We observed that the HER activity in alkaline media is clearly dependent on the exact AM^+ ($Li^+ > Na^+ > K^+$), which is consistent with previous studies^{20,22}. We further exploit a unique electrical transport spectroscopy (ETS) approach to directly probe the Pt-surface adsorbates at variable potentials, and electrochemical impedance spectroscopy (EIS) to study the near surface environment in the electrical double layer (EDL) and charge transfer resistance at the electrode-electrolyte interface. Based on these comprehensive on-surface and near-surface signals, we conduct density functional theory (DFT) calculations with explicit solvation, including static calculation, grand canonical DFT calculation, ab initio molecular dynamic (AIMD) simulation, and micro-solvation molecular cluster calculations, to develop molecular level insights into the surface adsorption properties, solvation structure, and the Pt-water interface dynamics in presence of cations and surface OH_{ad} species. Together, we experimentally and theoretically resolve the elusive role of AM⁺, and demonstrates AM⁺ plays an indirect role in modifying the adsorption strength and coverage of the hydroxyl species (OH_{ad}) (-OH_{ad@Li+} > -OH_{ad@Na+} > -OH_{ad@K+}) under the H_{upd}/HER potential regime, where the high OH_{ad} coverage with smaller AM⁺ promotes the HER activity. Specifically, our integrated studies reveal that Li⁺ cations less destabilize OH_{ad} on Pt surface (than Na⁺ and K⁺) and help retain more OH_{ad} that in turn act as both proton acceptors and donors to the nearby water molecules and facilitate the Volmer step kinetics and the HER activity in alkaline media (similar to the bifunctional mechanism), as also confirmed by greatly reduced charge transfer resistance observed in EIS studies. Our direct experimental and theoretical evidences provide critical fundamental insights into how and why AM⁺ influence the HER kinetics in alkaline media. It could enable an important vision for the design of future electrolyzers with improved energy efficiency and reduced cost.

Results

103

104

105

106

107

108

109

110

111

112

113

114

115

116

117

118

119

120

121

122

123

124

125

126

127

128

129

130

131132

Cation dependent HER activity and surface adsorbates

We have first examined the influence of cations by cyclic and linear scan voltammetry on Pt-disc electrode using conventional three electrode system in alkaline electrolytes at pH 13 with different AM⁺ (Li⁺, Na⁺, and K⁺). The cyclic voltammograms (CV) in the HER/HOR regime show that the H_{upd} peak shows a clear dependence on the exact AM⁺ (Fig. 1a). The peak potential is more positive in 0.1 M KOH and NaOH followed by 0.1 M LiOH (inset in Fig. 1a). A consistent and even more prominent trend has been previously observed on single crystal Pt surfaces by Koper and coworkers^{7,23}, in which H_{upd} peak was attributed not only to H adsorption but also to the replacement of OH_{ad} by H_{ad}²³. Thus, our work is in agreement with the previous reports that the negative peak shift with smaller AM⁺ is an indication that Li⁺ cations better stabilize (or less destabilize) OH_{ad} in the lower potential regime than Na⁺ and K⁺ cations. Linear scan voltammograms (LSV) demonstrate the highest HER activity was observed in case of Li⁺ followed by Na⁺ and K⁺ cations (Fig. 1b), also consistent with previous studies^{16,24}.

To understand the impact of these different AM^+ on the surface adsorbates in H_{upd}/HER regime, we have next exploited the ETS studies to directly probe the adsorbed species on the Pt surface. The ETS approach uses ultrafine PtNWs as a model catalyst^{25,26}, and involves a concurrent measurement of the PtNWs conductance during electrochemical studies at different electrochemical potentials (Fig. 2a) (See experimental section and ref.²⁵ for detailed working principle). The PtNWs (~ 2nm diameter) used in ETS studies show qualitatively similar CV and LSV results (Supplementary Fig. 1) with a consistent trend of AM^+ dependence to other types of Pt catalysts (e.g., Pt disc electrode).

Within the ETS approach, when the diameter (d) of the ultrafine PtNWs is smaller than the electron mean free path $(\lambda \sim 5 \text{ nm})^{27}$, their resistance is sensitively dependent on the surface adsorbates due to surface adsorbate induced scattering of the conduction electrons, producing a resistance change following equation 1 (ref.²⁵):

157
$$\rho = \rho_0 \left(\left(\frac{1-p}{1+p} \right) \times \frac{\lambda}{d} \right) \quad (d \ll \lambda)$$
 (1)

Here ρ and ρ_0 are the resistivity of the one-dimensional PtNWs and bulk metal respectively, λ is the mean free path of electron, d is the nanowire diameter, and p is a specularity parameter with a value ranging from 0 (for highly diffusive scattering) to 1 (completely specular scattering) (Fig. 2b)²⁷. The different surface adsorbate modifies the value of specularity (p) and thus the resistance

of the nanowires. It should be noted such surface scattering is exclusively sensitive to surface adsorbates, and not sensitive to the electrostatic or electrochemical potential. For example, previous studies have shown a constant conductance at different electrochemical potentials when there is a stable surface adsorbate layer (e.g., CO or I') that does not change with potential^{25,26}, confirming the insensitivity of the metallic PtNWs to the varying electrochemical potentials. Thus, the ETS approach offers a unique signal transduction pathway to exclusively probe the surface adsorbates, with little interference from the electrochemical potentials or the bulk electrolyte environment, which is difficult to achieve with other analytic approaches that are often convoluted with near surface (e.g., EDL) or bulk electrolyte background. Additionally, compared to interfacial-charge-transfer-based CV studies that cannot usually resolve surface adsorbates during active catalytic process (e.g., in HER potential regime) due to the dominance of much larger catalytic current over the surface adsorbate charge transfer, the ETS is exclusively sensitive to the surface adsorbates and insensitive to catalytic current. Thus, the ETS approach can allow to probe the surface adsorbates of active catalytic surfaces in action, which is essential for deciphering the catalytic molecular pathway.

We have first closely compared the ETS measurement with the corresponding the CV curve when the potential is gradually changed from 1.10 - 0.05 V vs. reversible hydrogen electrode (RHE) (Fig 2c), which consistently shows four distinct regions: (i) O/OH_{ad/des} region (1.10 - 0.60 V vs. RHE); (ii) electrical double layer region (OH_{ad} replaced by H₂O) (0.60 - 0.40 V vs. RHE); (iii) H_{upd} regime (0.40 - 0.08 V vs. RHE); and (iv) HER regime (0.08 - -0.05 V. RHE). The lowest conductance observed in the high potential regime is attributed to the larger scattering from the strongly bonded OHad on the Pt surface, which significantly reduces the conductance of the PtNWs. Scanning the potential toward lower potential regime results in a monotonic increase in conductance due to the gradual replacement of the OHad by H2O. The conductance increase slowed in the double layer regime where Pt surface are nearly completely reduced and most of the OH_{ad} are replaced by H₂O. Further sweeping the potential to the more negative regime results in H_{upd} on electrode surface (replacement of surface adsorbed H2O and residue OHad by Hupd), which further reduces scattering and increases conductance. The conductance eventually saturates at a nearly stable value below 0.15 V vs. RHE (beyond the H_{upd} peak in CV) due to a high coverage of adsorbed hydrogen. The ETS conductance measurement retains the nearly saturated conductance well into the HER regime (0.08 - -0.05 V vs. RHE), suggesting a largely similar surface adsorption

status in the HER regime. The derivative of the ETS shows two peaks near the potential regime where most OH desorption and H-adsorption occurs, which is largely consistent with CV curve and further highlights the validity of our approach and analysis (Supplementary Fig. 2).

We further compared the ETS data obtained with three different cations (Li^+ , Na^+ , and K^+). It was found the ETS data obtained with different cations show essentially the same conductance at high potential regime (1.10-1.00 V vs. RHE), suggesting a similar hydroxyl adsorption state at such potential. As we scan the potential towards lower potential regime, a notable conductance increase is observed in all cases, with a largely similar trend. However, it is interesting to note that the conductance increase is less pronounced with a smaller slope in the case of Li^+ cations as compared to that of Na^+ and K^+ (Fig. 2d). Considering the conductance increase is primarily resulted from the replacement of OH_{ad} by H_2O and then by H_{upd} , the smaller increase in conductance in the presence of Li^+ cations suggests that less OH_{ad} are being desorbed or replaced by H_2O or H_{ad} when compared that with the other larger cations (Na^+ and K^+ cations). We note that the difference among these three cations persist throughout the entire potential regime down -0.05V vs. RHE, suggesting different extent of OH_{ad} remained on the Pt in the H_{upd}/HER potential window.

Theoretical insight into the role of cations on surface adsorbates

Although it has been commonly perceived that OH_{ad} may not be stable in the H_{upd}/HER potential regime, there are occasional suggestions that some level of OH_{ad} may persist in this potential regime^{7,8}, which is consistent with our ETS studies. To understand these experimental findings, we performed theoretical studies to investigate the extent of OH_{ad} in presence of different cations. To gain insight into how and why different cations influence the surface adsorption property, density functional theory (DFT) calculations are performed on the Pt(111)-water interface, which is modeled by the Pt(111) slab covered by an explicit water layer (Supplementary Fig. 3). The DFT optimized geometries are shown in Supplementary Fig. 4. The adsorption energy of OH_{ad} (E_{ad}^{OH}) on the Pt(111) is calculated to be -3.46 eV, -2.81 eV, and -2.32 eV (see below for the estimation of statistical fluctuations from solvent dynamics) in the presence of Li⁺, Na⁺, and K⁺, respectively (Fig. 3a). Compared to the case of pure water environment (-3.50 eV), the presence of cations would destabilize the OH_{ad} , and the extent of such destabilization follows the trend of K⁺ > Na⁺ > Li⁺. Grand canonical DFT calculations (Fig. 3b) confirm that this trend persists

for potential-dependent adsorption free energy of OH (G_{ad}^{OH}) throughout the entire electrochemical window (-1.0 to 1.0 V vs. RHE), and the OH_{ad} is favorable even under a more negative potential.

Our DFT calculations show that the adsorption strength of OH_{ad} follows the order of $Li^+>Na^+>K^+$, which is consistent with the experimental observations in ETS studies (Fig. 2d). To understand the origin of such difference in adsorption strength, we further calculated the electron density difference ($\Delta\rho_e$) at the Pt(111)-water interface after introducing different cations. Overall, the interaction between the cation and the OH_{ad} is mostly electrostatic (decays in inverse square law) and its effect on the electronic structure of Pt surface is mild. The yellow isosurfaces between cation and nearby water show the electron density redistribution on water to form cation-water bond, and a larger lobe suggests a higher extent of such redistribution (Fig. 3d-f). The more dramatic electron density redistribution in the presence of Li^+ can be attributed to the stronger local electric field from its highest charge density (same net charge but much smaller ionic radius), compared to Na^+ and K^+ . The electric field exerted by the cation also causes electron density redistribution in the OH_{ad} , reducing the electron density of the lone pair closest to the cation (region A in insets) while increasing for the farther lone pair (region B in insets). It is interesting to note that the region corresponding to Pt-O bond (region C in insets) also experiences an increase in electron density, which is due to charge compensation from bulk Pt to the polarized OH_{ad} .

To further quantify such polarization and charge redistribution of OH_{ad} , we performed Bader charge analysis on the interface (Supplementary Fig5), and the net charge on O in OH_{ad} is calculated to be -0.52 |e|, -0.49 |e|, and -0.48 |e| in presence of Li^+ , Na^+ , and K^+ , respectively. Based on Bader charges, the dipole moment of the O- H_{ad} (Pt-O) are calculated to be 2.37 D, 2.19 D, and 2.15 D (2.09 D, 1.69 D and 1.06 D) for Li^+ , Na^+ , and K^+ (Fig. 3c), respectively. Hence, it is clear that the extent of charge redistribution and polarization of OH_{ad} both follow the trend of $Li^+ > Na^+ > K^+$, which is likely caused by stronger electric field of Li^+ , analogous to polarization of the first hydration sphere.

Since the hydration sphere and water configuration at the Pt-water interface is not static, we further performed ab initio molecular dynamics (AIMD) simulations at the Pt(111)-water interface with near-surface hydrated cations in the canonical ensemble at 300 K to account for the dynamics and better sample the configurational space. A 100 ps trajectory is obtained for each system after pre-equilibration, with a variance of potential energy to be within 0.15 eV, marking proper

equilibration of the system (Supplementary Fig. 6). The cation-oxygen radial distribution function (RDF) (Supplementary Fig. 7) obtained from the AIMD trajectory are consistent with the result of large-scale molecular mechanics (MM) simulation²⁸ and test simulations with a larger cell size or thicker water layer (Supplementary Note 1), demonstrating the correct hydration structure of the cations. The adsorption enthalpy (approximated by MD average of potential energy) of OH (\widetilde{E}_{ad}^{OH}) is calculated to be -2.71 eV, -2.51 eV, and -2.40 eV in presence of Li⁺, Na⁺, and K⁺, respectively (Fig. 3a), which is largely consistent with the trend of the E_{ad}^{OH} and potential-dependent G_{ad}^{OH} calculated for static models (Fig. 3a,b), further confirming more favorable OH_{ad} in the presence of Li⁺.

253

254

255

256

257

258

259

260

261

262

263

264

265266

267

268

269

270

271

272

273

274

275

276

277

278

279

280

281

282

283

The reduction of the adsorption energy (Fig. 3a) with increasing AM⁺ size (from Li⁺, Na⁺, to K⁺) is contributed by the interface dynamics. We note it has been a debated topic whether cations directly adsorb or simply accumulate in the outer-Helmholtz plane in the double layer²⁹⁻³¹. Hence, we further studied the cation dynamics and its hydration structure. The representative snapshot of each system at equilibrium and at the position closest to the surface (Supplementary Fig.8) shows that the cation stays in the double layer most of the time, oscillating between the first and second water layers. During the 100 ps AIMD simulation, Li⁺ maintains a coordination number (CN) of 4 and oscillates in the upper half between the first and second water layer. The CN fluctuates between 4 and 5 for Na⁺ and oscillates in the lower half between the first and second water layer. On the other hand, K⁺ doesn't have a specific CN, and frequently penetrates the first water layer but never stays specifically adsorbed on the Pt surface. The cation coordination numbers (4 for Li^+ , ~4-5 for Na⁺, ~4-6 for K⁺) obtained in our simulation are consistent with ref³², and the position of cations is consistent with ref³¹. The averaged distance between the cation and Pt(111) surface are 4.44 Å, 4.42 Å, and 3.95 Å without surface OH and 5.38 Å, 4.43 Å, and 3.88 Å with surface OH, respectively, which is due to different rigidness of their hydration sphere as also characterized by the sharpness of RDF peak (Supplementary Fig. 7). Notably, only Li⁺ is observed to have a well-defined second hydration sphere, and only K⁺ experiences instantaneous penetration of water inside its first hydration shell (Supplementary Fig.7). The variation in cation-surface distance partially smears the difference in OH adsorption for different cations, while leaving the overall trend qualitatively unchanged. The distinct interfacial dynamics are attributed to the different charge density of the cations, cation-water interaction strength, and the mass of the cations (heavier cations are less dragged by the friction of its water environment). It is noted that the observation

that the cations do not stay dehydrated and form bonds with the Pt surface contradicts the hypothesis previously proposed in ref^{7,30,33,34}, whose discrepancy is likely a result of undercoordination of the cations from insufficient explicit solvation, which leads to the overestimation of cation-surface binding strength. We also note that previous studies indicated large cations (e.g., Cs⁺) may show a stronger interaction and direct adsorption on electrode surface due to less tightly bounded solvation shell in large cations²⁴. Indeed, our preliminary ETS studies also suggested that the larger cations (Rb⁺ or Cs⁺) may directly adsorb on electrode surface (Supplementary Note 2) and are expected to influence the HER activity in a very different way. Therefore, we excluded the Rb⁺ and Cs⁺ ions from this study.

Cation modulation of local chemical environment and HER kinetics

The aforementioned experimental ETS results and theoretical calculations confirm that the AM^+ don't specifically adsorb on the electrode surface but instead accumulate in outer-Helmholtz plane. To probe the distribution of cations in the outer-Helmholtz plane of the EDL, we performed electrochemical impedance spectroscopy (EIS) analysis in different cation electrolytes and determined the double layer capacitance (C_{dl}) at different applied potentials (Fig. 4a). In the simplified equation, the C_{dl} is directly related to the relative permittivity (ϵ) of the solvent at constant electrolyte concentration (C) as shown below 35 .

$$C_{dl} = \varepsilon \varepsilon_o \sqrt{C}$$
 (2)

The EIS studies reveal a larger C_{dl} in the high potential regime (1.1-0.6 V vs. RHE) for K^+ than for Na^+ and Li^+ , which can be attributed to lower hydration energy, shorter cation-surface distance, and less rigid hydration sphere (hence a smaller effective hydration sphere radius) of K^+ as compared to Na^+ and Li^+ ³⁶. However, an opposite trend was observed when the potential goes into H_{upd}/HER regime, showing a larger C_{dl} in case of Li^+ . This reversal in C_{dl} is attributed to the change in local cation concentration induced by the change in surface species. With the interaction between hydrated cation and surface OH_{ad} shown in our DFT calculations, we hypothesize that local cation concentration might be highly dependent on the coverage and polarity of surface OH_{ad} , and might be substantially different from the bulk concentration.

To further explore how the surface OH_{ad} and near-surface cations influence the dynamic properties of each other, we analyze the AIMD trajectories of Pt(111)-water and Pt(111)-OH_{ad}-water with near-surface hydrated cations. The first peak in RDF of Pt-O (Fig. 4b) corresponds to

Pt-OH bond, and is the leftmost and sharpest in presence of Li⁺ followed by Na⁺ and K⁺, suggesting the strongest Pt-OH bond with Li⁺ and consistent with experimental and theoretical results discussed in the previous sections. The second peak corresponds to the first water layer, and it is about the same for three cations, showing consistent distribution of near-surface water independent on identity of the hydrated cations.

Interestingly, the polarized OH_{ad} in turn could stabilize the hydrated cations to stay in its surrounding. The root-mean square deviation (RMSD) of the Li^+ position from the Pt surface shows considerably larger fluctuation in absence of OH_{ad} (Fig. 4c), suggesting large and frequent oscillation and drifting of Li^+ away from its equilibrium position (zero reference). After introducing OH_{ad} , the RMSD flattens and seldom goes beyond 1.5 Å from the equilibrium position, suggesting an anchoring of Li^+ cations to the Pt surface by OH_{ad} . A similar anchoring effect is also observed for Na^+ and K^+ ions, although to a less extent due to weaker cation-OH interactions (Supplementary Fig. 9). We note such anchoring differs from the specific adsorption since the cation and OH_{ad} is separated by the first hydration shell (ca. 4 Å apart) without forming any direct cation-OH bond or OH_{ad} -induced dehydration (Supplementary Note 3), which differs from the work by Koper and Janik despite a similar trend ^{7,8}. Since the OH_{ad} has the higher surface coverage and polarity in presence of Li^+ followed by Na^+ and K^+ , which means more anchors and stronger anchoring effect, leading to a higher local concentration of cations ($Li^+ > Na^+ > K^+$) near the Pt surface.

To conclude, the crossover of C_{dl} in the EIS near 0.60 V vs. RHE is induced by the change in surface coverage of OH_{ad} : (1) at higher potential (>0.60 V vs. RHE) where there are abundant surface OH_{ad} , the capacitance ($K^+ > Na^+ > Li^+$) is more determined by the inverse of cation-surface distance and hydration sphere size; (2) at lower potential (<0.60 V vs. RHE) when there is only a limited number of OH_{ad} , the capacitance ($Li^+ > Na^+ > K^+$) is more dictated by the local cation concentration which is in turn related to coverage of the remaining OH_{ad} due to its anchoring effect.

The charge transfer resistance was also determined from EIS data. The electrode-electrolyte interface was largely capacitive in the entire potential range except the HER region (Fig. 4d). The charge transfer resistance is the opposition experienced for electron movement at electrode-electrolyte interface. The charge transfer resistance in the oxidation region (~1V) is not meaningful as it is largely capacitive with a minimal charge transfer process. However, in the hydroxyl

desorption potential regime (\sim 0.9-0.4V vs. RHE), the charge transfer resistance is larger for Li⁺ ions when compared to Na⁺ and K⁺ ions, suggesting more difficult desorption of OH_{ad} and replacement by H₂O molecules in presence of Li⁺ ions, consistent with our ETS results. While in the H_{upd} and HER regime (<0.4 V vs. RHE), the charge transfer resistance is lowest for Li⁺ ions followed by Na⁺ and K⁺ ions, consistent with the improved Volmer step kinetics for H_{upd} and HER for Li⁺ ions followed by Na⁺ and K⁺ ions (Fig. 1b).

To further understand the HER activity trend, we focus on the behavior of water molecules in the AIMD because water is the major proton source in alkaline HER. With the alkaline Volmer step (involving water dissociation) being the rate determining step ¹³, the O-H bond strength in near-surface water could work as a metric explaining HER activity. To this end, we examined the RDF of O-H of water in the surrounding of different species (Fig. 5a). Compared to the water in the regular bulk water environment, the water O-H bond length in the first hydration shell of cation experiences a downshift of the peak position and a slight sharpening of the peak, suggesting the strengthening of the O-H bond of water in the hydration shell of cations. On the other hand, the O-H peak of water molecules next to both O and H of OH_{ad} show a longer tail on the stretching side (~1.05 - 1.1 Å), indicating that OH_{ad} can function as both proton acceptors and donors to weaken O-H bond in nearby water, hence leading to a lower barrier for water dissociation.

coordination number of O by H (Fig. 5c), is smaller than the case of bulk water probably due to blockage of H-bond sites by the steric hindrance of the Pt surface.

The water near the H in OH_{ad} (with OH_{ad} being H-bond donor) has a similar peak height/area to that in bulk water (Fig. 5b), indicating a similar hydrogen bond strength. The Bader charge analysis indicates that there is less positive charge on H in OH_{ad} (0.04 |e| for H in OH_{ad} vs. ~ 0.1 |e| on H in water), the surface OH_{ad} is thus an electronically weaker H-bond donor. On the other hand, the longer tail in the O-H stretching region for water near H in OH_{ad} (Fig. 5a inset) indicates the OH_{ad} does function as a proton donor to weaken O-H in nearby water molecules, which is likely due to synergistic geometric effect of the surface bound OH_{ad} and near Pt-surface water dynamics.

Together, by combining systematic experimental and theoretical studies, we reveal that the cations play an indirect role in alkaline HER on Pt. It is the enhanced surface concentration of OH_{ad} induced by presence of smaller cations (Li⁺), instead of the cation itself, that enhances the HER activity in alkaline media (Fig. 5d). The smaller cations lead to a higher OH_{ad} coverage on Pt surface in the HER potential window, which can act as an electronically favored proton acceptors and geometrically favored proton acceptors to promote water dissociation and the Volmer step kinetics in alkaline media. The higher OH_{ad} coverage in case of Li⁺ ions (followed by Na⁺ and then K⁺) leads to the higher HER activity.

We note in our finding that cations stabilize its first hydration shell is to the very contrary of the common perception that the cations can directly activate its hydration sphere ^{33,37}, and hence we performed a sanity check with a finer micro-solvation model at a higher level of theory and evaluated Mayer bond order (BO) of the O-H bonds based on DFT-optimized geometries (Fig. 5e,f). Without explicit solvation, the Mayer bond order of H-O in the hydration shell of Li⁺ (0.906) is lower than that of an isolated water (0.949), resulting from polarization by the electrostatics of the cation. Interestingly, the trend is reversed when the system is subject to explicit solvation. In a H-bond network, each water molecule is connected to four neighboring water molecules via H-bond, which causes a significant weakening of the O-H bond in water to result in a Mayer BO of 0.808. However, each water molecule in the first hydration shell of Li⁺ can only connect to 2 or 3 neighboring water molecules due to the blockage of H-bond sites by the steric effect of the cation. The Mayer bond order of the O-H in the hydration shell of cation (0.827) is therefore weakened to

a lesser extent since the effect of water environment outcompetes the effect of cations. In other words, the water in the hydration shell of cation is stabilized compared to the water in bulk water. Hence, the argument of cation activating its hydration sphere is likely a victim of underestimating the role of the water environment. We recognize that the models adopted in this study have certain limitations in various aspects due to computation-cost limitations (see details in Supplementary Note 4), we believe this example well highlights the necessity of including sufficient explicit solvation to properly describe the reactivity of water both in bulk solution and at an electrochemical interface.

Conclusions

In conclusion, we have combined a unique surface-adsorbate exclusive electrical transport spectroscopy (ETS) approach with the electrochemical impedance spectroscopy (EIS) and DFT calculations to directly probe the on-surface and near-surface chemical environment, deciphering the elusive role of AM⁺ on Pt surface chemistry and alkaline HER. Our integrated studies suggest that the cation is not directly bonded to the Pt surface or OH_{ad}, but separated by a water molecule in the first hydration shell of the cation, distinct from previous studies⁷. Moreover, the smaller cations favor higher OH_{ad} coverage on Pt surface in the HER potential window, which in turn function as electronically favored proton acceptors or geometrically favored proton donors to promote water dissociation and the Volmer step kinetics on Pt surface in alkaline media, leading to improved HER activity in the presence of smaller cations (Li⁺). Our studies resolve the fundamental role of AM⁺ in HER kinetics that has remained elusive in recent decades, and could offer valuable insights for the design of more efficient electrolyzers for renewable energy conversion.

Methods

Chemicals

Lithium hydroxide (LiOH, >98%), sodium hydroxide (NaOH, 98%), potassium hydroxide (KOH, 87.4%), and perchloric acid (HClO4, 70%, PPT grade) were all purchased from Thermo Fisher Scientific. All aqueous solutions were prepared using deionized (DI) water (18.2 M Ω ·cm) obtained from an ultrapure purification system (Aqua Solutions).

Electrochemical Measurements

All of the electrochemical measurements were performed using typical three electrode setup. Platinum rotating disk was used as working electrode, Pt wire and Ag/AgCl were used as the counter and reference electrodes, respectively. All of the potentials reported are versus reversible hydrogen electrode (RHE), calibrated in the same electrolyte by measuring the potential of the HOR/HER currents at zero corresponding to 0 V versus RHE (VRHE).

Impedance Measurements

433

434

435

436

437

438

439

440

441

442

443

451

456

The impedance spectra were measured with frequencies from 10^5 to 1 Hz with an amplitude of 10 mV_{rms} at different applied voltages. CV were conducted between each potential to avoid any influence from the surface passivation. Equivalent circuits were fitted to the data with aftermath software.

Synthesis of Pt nanowires (PtNWs)

- The PtNWs for ETS measurements were synthesized by following previously reported protocol ³⁸.
- Briefly, 20 mg of Pt(acac)₂, 30 mg of Ni (acac)₂, 1.6 mg of W(CO)₆, 135 mg of glucose and 60 mg
- of PVP (mw. 40,000) were dissolved in 2 mL of 1-octadecene (ODE) and 3 mL oleylamine (OAm).
- After sonicating for 15 min, the solution was sealed with argon. The mixture was then heated up
- 448 to 140 °C for 4 hours. The product was centrifuged by ethanol for 15 minutes, followed by
- cyclohexane for 20 minutes. Finally, product was centrifuged in the mixture of 5 mL cyclohexane
- and 15 mL ethanol for 20 minutes. Final product was dispersed in ethanol for device preparation.

Preparation of PtNW films

- A free standing PtNW film was assembled on chip from as-prepared PtNW suspension by a co-
- solvent evaporation method ²⁵. Briefly, PtNW suspensions in ethanol (400 ul, 0.4 mg ml⁻¹) was
- added dropwise into a beaker (about 9 cm in diameter) filled with DI water. A thin film of PtNWs
- from top of water surface was then transferred onto the device.

Fabrication of the PtNW electrochemical device

- The device fabrication was followed by the similar approach as previously reported by our group
- 458 ²⁵. Typically, a PMMA (A8, MicroChem Corp.) film was prepared by spin coating on the substrate
- 459 (p++ silicon wafer with 300 nm thermal oxide) surface with pre-patterned Au electrodes (Ti/Au,
- 460 50/50 nm). E-beam lithography was then used to open windows on PMMA, which created desired
- patterns on the substrate. After the removal of PMMA template, PtNWs was deposited on the

device substrate with desired patterns. To rule out the influence of electrolyte and to avoid electrochemical reactions on the Au electrodes, another layer of PMMA (~500-nm thick, electrochemically inert) was then deposited on the PtNW device with spin coating. A smaller window that only exposes PtNWs was opened by e-beam lithography. The device was finally used for in-device electrochemistry and in situ electrical transport spectroscopy measurement.

In-device CV and in situ ETS

462

463

464

465

466

467

474

- A two channel SMU (Agilent B2902a) was used for the measurement. The first SMU channel was used as a potentiostat to control the potential of source electrode as to the reference electrode (V_G),
- while collecting the current (I_G) through the counter electrode with a scan rate of 50 mV/sec. The
- SR830 Lock-In Amplifiers from Stanford research system was used to supply a small sinusoidal
- current (10 µA) between source and drain electrodes and collecting the corresponding voltage
- 473 (V_{SD}) . Source drain voltage (V_{SD}) was then used to measure the conductance.

Slab model set-up and DFT methods

- The Pt/water interface is modeled by a Pt (111) slab and an explicit water slab on top of it. The Pt
- slab is a 3-layer 4x4 supercell of Pt(111) termination with an area of 1.10 nm². The explicit water
- slab is 6 Å thick, containing 22 water molecules (estimated from the water density of 1.0 g/cm³ at
- 478 room temperature). The bottom two layers of the Pt slab are constrained as bulk region, and
- everything else are allowed to relax as the interface region. A vacuum slab of 10 Å thickness is
- added in Z direction to avoid spurious interactions between periodic images.
- 481 The solvation configuration for production run is sampled by random placement of water
- 482 molecules in the water slab region followed by local optimization at DFT level, with a sampling
- 483 size of 50 configurations, using our open-source Python package GOCIA
- 484 (https://github.com/zishengz/gocia). Cation is introduced by replacing a water molecule and then
- re-optimizing the geometry. Surface OH_{ad} is introduced by placing a OH species onto the Pt
- surface and then re-optimizing the geometry. Although our calculations use Pt(111) as a model
- system, we expect similar conclusion holds true for other surfaces and it is noted that the stepped
- surfaces have even more favorable OH_{ad} compared to Pt(111) terrace¹⁹.
- The geometry optimizations are performed with the PBE functional³⁹ and PAW pseudopotentials⁴⁰
- using the VASP program (version 5.4.1) 41-44. D3 correction is used to better account for the

dispersion interactions ⁴⁵. The convergence criteria for geometry (SCF) are set to 10^{-5} eV for energy and 0.02 eV/Å for forces. Due to the relatively large system and sampling size, only the Γ k-point is sampled in the reciprocal space of the Brillouin zone throughout, and the cutoff energy for the kinetic energy of the plane-waves was 400 eV. The Bader charges are calculated from the charge density output using Bader Charge Analysis code⁴⁶.

Grand canonical DFT calculations

Under a constant applied potential, the electrode surface is effectively a grand canonical ensemble where the number of electrons is varied to adapt to the change in the work-function of the surface (caused by adsorbates or near surface species). The potential-dependent electronic free energy of the surface can be approximated using the surface charging method⁴⁷:

501
$$G(U) = E(U) - q(U) \cdot FU \approx E(U_0) - \frac{1}{2}C(U - U_0)^2$$
 (3)

Here, E(U) is the electronic energy of the surface under a potential U which is calculated by referencing the Fermi level of the system against the vacuum level. q(U) is the surface charge difference referenced against the neutral system, and F is the Faradaic constant. U_0 stands for the potential of zero charge in vacuum scale, and C is the effective capacitance of the electrochemical interface. By varying the number of electrons in the system, the E(U) of the system at the corresponding U and q(U) can be obtained, and thereby a parabolic relation between G(U) and U can be fitted by sampling a series of Q values. The U (in vacuum scale) can be converted into the RHE scale by referencing it against the experimental U_{SHE} (4.44 V) ⁴⁸ and adding a pH correction of $0.0592 \times pH$.

Ab initio molecular dynamics

The ab initio molecular dynamics simulations are performed on the optimized structures with the same DFT setting as the geometry optimization using the VASP program (version 5.4.1). The simulation is performed in the NVT (canonical) ensemble at 300 K with the Nose-Hoover thermostat. The time step is set to 1 fs, and 100 ps trajectory after the equilibration of the system is collected for analysis. Multiple independent simulations starting with different height of cation are performed and we observe little dependence of the obtained equilibrium on the initial conditions. The radial distribution function analysis is performed using the VMD program (version 1.9.4a48)⁴⁹.

Calculation of adsorption energies

520

532

544

The adsorption energy of OH on the surface to form OH_{ad} is calculated by:

522
$$E_{\text{ads}}^{\text{OH}} = E(* \text{ OH}_{\text{ad}}) - E(*) - E(\text{OH})$$
 (4)

- Here, the energy E is from the static calculation on a single configuration. The * stands for the
- Pt/water interface, and OH stands for an isolated OH species (from implicit solvation calculation
- or experimentally determined solvation free energy, see Supplementary Note 5).
- The static DFT energy E can be replaced by the trajectory-averaged potential energy \tilde{E} from the
- 527 AIMD simulation to yield the trajectory-averaged adsorption enthalpy:

528
$$\tilde{E}_{\text{ads}}^{\text{OH}} = \tilde{E}(* \text{ OH}_{\text{ad}}) - \tilde{E}(*) - E(\text{OH})$$
 (5)

- We can also replace E with the potential-dependent free energy G(U) to yield the potential-
- 530 dependent free energy of adsorption:

531
$$G_{ads}^{OH}(U) = G(U; *OH_{ad}) - G(U; *) - E(OH)$$
 (6)

Micro-solvation model set-up and DFT methods

- The isolated form of hydrated cations are $Li(H_2O)_4^+$, $Na(H_2O)_5^+$, and $K(H_2O)_6^+$, which are typical
- 534 hydration structures taken from ref.³². The outer-shell solvation configuration around the water
- and hydrated cations are sampled as a micro-solvation molecular cluster by random placement of
- water molecules within a spherical region of 7 Å radius (around the species to be solvated)
- followed by local optimization at DFT level, with a sample size of 50 configurations, using the
- Genmer module in the Molclus program⁵⁰.
- The geometry optimizations are performed with B3LYP functional^{51,52} and def-TZVP basis sets⁵³
- using the Gaussian 16 program⁵⁴ (Revision C.01). D3 correction⁴⁵ with Becke-Johnson damping
- 541 55 is used to better account for the dispersion interactions. Hirshfeld population analysis and Mayer
- bond order analysis is performed using the Multiwfn program⁵⁶ on the converged wavefunctions
- 543 from DFT calculation.

Data availability

- The data that support the plots within this paper and other findings of this study are available from
- the corresponding author upon reasonable request. The DFT-optimized geometries and AIMD
- trajectories are available at https://doi.org/10.5281/zenodo.7026971.

References

548

- 549 1 Sheng, W., Gasteiger, H. A. & Shao-Horn, Y. Hydrogen oxidation and evolution reaction
- kinetics on platinum: acid vs alkaline electrolytes. J. Electrochem. Soc. 157, B1529-B1536 (2010).
- Li, L., Wang, P., Shao, Q. & Huang, X. Recent Progress in Advanced Electrocatalyst Design
- 552 for Acidic Oxygen Evolution Reaction. Adv. Mater. **33**, 2004243-2004266, (2021).
- Gasteiger, H. A., Panels, J. E. & Yan, S. G. Dependence of PEM fuel cell performance on
- catalyst loading. J. Power Sources. **127**, 162-171 (2004).
- Nørskov, J. K. et al. Trends in the exchange current for hydrogen evolution. J. Electrochem.
- 556 Soc. **152**, J23-J26 (2005).
- 557 5 Zhang, W. et al. WO_x-Surface Decorated PtNi@Pt Dendritic Nanowires as Efficient pH-
- 558 Universal Hydrogen Evolution Electrocatalysts. Adv. Energy Mater. 11, 2003192-2003198
- 559 (2021).
- 560 6 Sheng, W., Myint, M., Chen, J. G. & Yan, Y. Correlating the hydrogen evolution reaction
- activity in alkaline electrolytes with the hydrogen binding energy on monometallic surfaces.
- 562 Energy Environ. Sci. 6, 1509-1512 (2013).
- 563 7 Chen, X., McCrum, I. T., Schwarz, K. A., Janik, M. J. & Koper, M. T. M. Co-adsorption of
- Cations as the Cause of the Apparent pH Dependence of Hydrogen Adsorption on a Stepped
- Platinum Single-Crystal Electrode. Angew. Chem. Int. Ed. **56**, 15025-15029 (2017).
- McCrum, I. T., Chen, X., Schwarz, K. A., Janik, M. J. & Koper, M. T. M. Effect of Step
- Density and Orientation on the Apparent pH Dependence of Hydrogen and Hydroxide Adsorption
- on Stepped Platinum Surfaces. J. Phys. Chem. C. **122**, 16756-16764 (2018).
- 569 9 Ledezma-Yanez, I. et al. Interfacial water reorganization as a pH-dependent descriptor of the
- 570 hydrogen evolution rate on platinum electrodes. Nat. Energy. **2**, 17031 (2017).
- 571 10 Seto, K., Iannelli, A., Love, B. & Lipkowski, J. The influence of surface crystallography on
- the rate of hydrogen evolution at Pt electrodes. J. Electroanal. Chem. Interf. Electrochem. 226,
- 573 351-360 (1987).
- 574 11 Markovića, N. M., Sarraf, S. T., Gasteiger, H. A. & Ross, P. N. Hydrogen electrochemistry
- on platinum low-index single-crystal surfaces in alkaline solution. J. Chem. Soc. Faraday Trans.
- **92**, 3719-3725 (1996).

- 577 12 Marković, N., Grgur, B. & Ross, P. N. Temperature-dependent hydrogen electrochemistry on
- 578 platinum low-index single-crystal surfaces in acid solutions. J. Phys. Chem. B. 101, 5405-5413
- 579 (1997).
- 580 13 Subbaraman, R. et al. Enhancing Hydrogen Evolution Activity in Water Splitting by Tailoring
- 581 Li⁺-Ni(OH)₂-Pt Interfaces. Science **334**, 1256-1260 (2011).
- 582 14 Subbaraman, R. et al. Trends in activity for the water electrolyser reactions on 3d
- 583 M(Ni,Co,Fe,Mn) hydr(oxy)oxide catalysts. Nat. Mater. **11**, 550-557 (2012).
- Li, J. et al. Experimental Proof of the Bifunctional Mechanism for the Hydrogen Oxidation in
- 585 Alkaline Media. Angew. Chem. Int. Ed. **56**, 15594-15598 (2017).
- Liu, E. et al. Unifying the Hydrogen Evolution and Oxidation Reactions Kinetics in Base by
- Identifying the Catalytic Roles of Hydroxyl-Water-Cation Adducts. J. Am. Chem. Soc. 141, 3232-
- 588 3239 (2019).
- 589 17 Cong, Y. et al. Uniform Pd_{0.33}Ir_{0.67} nanoparticles supported on nitrogen-doped carbon with
- remarkable activity toward the alkaline hydrogen oxidation reaction. J. Mater. Chem. A. 7, 3161-
- 591 3169 (2019).
- 592 18 Qiu, Y. et al. BCC-Phased PdCu Alloy as a Highly Active Electrocatalyst for Hydrogen
- 593 Oxidation in Alkaline Electrolytes. J. Am. Chem. Soc. **140**, 16580-16588 (2018).
- 594 19 McCrum, I. T. & Koper, M. T. M. The role of adsorbed hydroxide in hydrogen evolution
- reaction kinetics on modified platinum. Nat. Energy. **5**, 891-899 (2020).
- 596 20 Xue, S. et al. Influence of Alkali Metal Cations on the Hydrogen Evolution Reaction Activity
- of Pt, Ir, Au, and Ag Electrodes in Alkaline Electrolytes. ChemElectroChem. 5, 2326-2329 (2018).
- 598 21 Monteiro, M. C. O., Goyal, A., Moerland, P. & Koper, M. T. M. Understanding Cation Trends
- for Hydrogen Evolution on Platinum and Gold Electrodes in Alkaline Media. ACS Catal. 11,
- 600 14328-14335 (2021).
- Weber, D., Janssen, M. & Oezaslan, M. Effect of monovalent cations on the HOR/HER
- activity for Pt in alkaline environment. J. Electrochem. Soc. **166**, F66-F73 (2019).
- van der Niet, M. J. T. C., Garcia-Araez, N., Hernández, J., Feliu, J. M. & Koper, M. T. M.
- Water dissociation on well-defined platinum surfaces: The electrochemical perspective. Catal.
- 605 Today **202**, 105-113 (2013).
- 606 24 Huang, B. et al. Cation- and pH-Dependent Hydrogen Evolution and Oxidation Reaction
- 607 Kinetics. JACS Au. 1, 1674-1687 (2021).
- Ding, M. et al. An on-chip electrical transport spectroscopy approach for in situ monitoring
- electrochemical interfaces. Nat. Commun. 6, 7867 (2015).
- 610 26 Ding, M. et al. On-chip in situ monitoring of competitive interfacial anionic chemisorption as
- a descriptor for oxygen reduction kinetics. ACS Cent. Sci. 4, 590-599 (2018).

- 612 Yoo, H.-W., Cho, S.-Y., Jeon, H.-J. & Jung, H.-T. Well-Defined and High Resolution Pt
- Nanowire Arrays for a High Performance Hydrogen Sensor by a Surface Scattering Phenomenon.
- 614 Anal. Chem. 87, 1480-1484 (2015).
- 615 28 Kiyohara, K. & Minami, R. Hydration and dehydration of monovalent cations near an
- electrode surface. J. Chem. Phys. **149**, 014705-014714 (2018).
- 617 29 Rebollar, L. et al. "Beyond Adsorption" Descriptors in Hydrogen Electrocatalysis. ACS Catal.
- **10**, 14747-14762 (2020).
- 619 30 Mills, J. N., McCrum, I. T. & Janik, M. J. Alkali cation specific adsorption onto fcc(111)
- transition metal electrodes. Phys. Chem. Chem. Phys. 16, 13699-13707 (2014).
- Ringe, S. et al. Understanding cation effects in electrochemical CO₂ reduction. Energy
- 622 Environ. Sci. 12, 3001-3014 (2019).
- 623 32 Mähler, J. & Persson, I. A Study of the Hydration of the Alkali Metal Ions in Aqueous
- 624 Solution. Inorg. Chem. **51**, 425-438 (2012).
- 625 33 McCrum, I. T. & Janik, M. J. First Principles Simulations of Cyclic Voltammograms on
- Stepped Pt(553) and Pt(533) Electrode Surfaces. ChemElectroChem. 3, 1609-1617 (2016).
- 627 34 McCrum, I. T. & Janik, M. J. pH and Alkali Cation Effects on the Pt Cyclic Voltammogram
- 628 Explained Using Density Functional Theory. J. Phys. Chem. C. 120, 457-471 (2016).
- 629 35 Lust, E. Electrical Double Layers. Double Layers at Single-crystal and Polycrystalline
- Electrodes. In Encyclopedia of Electrochemistry; Bard, A. J., Eds., Wiley, 2002.
- 631 36 Garlyyev, B., Xue, S., Watzele, S., Scieszka, D. & Bandarenka, A. S. Influence of the Nature
- of the Alkali Metal Cations on the Electrical Double-Layer Capacitance of Model Pt(111) and
- 633 Au(111) Electrodes. J. Phys. Chem. Lett. **9**, 1927-1930 (2018).
- 634 37 Goyal, A. & Koper, M. T. Understanding the role of mass transport in tuning the hydrogen
- evolution kinetics on gold in alkaline media. J. Chem. Phys. **155**, 134705-134715 (2021).
- 636 38 Li, M. et al. Ultrafine jagged platinum nanowires enable ultrahigh mass activity for the oxygen
- reduction reaction. Science **354**, 1414-1419 (2016).
- 638 39 Adamo, C. & Barone, V. Toward reliable density functional methods without adjustable
- parameters: The PBE0 model. J. Chem. Phys. **110**, 6158-6170 (1999).
- 640 40 Kresse, G. & Joubert, D. From ultrasoft pseudopotentials to the projector augmented-wave
- method. Phys. Rev. B. **59**, 1758-1775 (1999)
- 642 41 Kresse, G. & Furthmüller, J. Efficiency of ab-initio total energy calculations for metals and
- semiconductors using a plane-wave basis set. Comput. Mater. Sci. 6, 15-50 (1996).
- Kresse, G. & Furthmüller, J. Efficient iterative schemes for ab initio total-energy calculations
- using a plane-wave basis set. Phys. Rev. B. **54**, 11169-11186 (1996).

- 646 43 Kresse, G. & Hafner, J. Ab initio molecular dynamics for liquid metals. Phys. Rev. B. 47,
- 647 558-561 (1993).
- 648 44 Kresse, G. & Hafner, J. Ab initio molecular-dynamics simulation of the liquid-metal-
- amorphous-semiconductor transition in germanium. Phys. Rev. B. 49, 14251-14269 (1994).
- 650 45 Grimme, S., Antony, J., Ehrlich, S. & Krieg, H. A consistent and accurate ab initio
- parametrization of density functional dispersion correction (DFT-D) for the 94 elements H-Pu. J.
- 652 Chem. Phys. **132**, 154104-1541023 (2010).
- 46 Yu, M. & Trinkle, D. R. Accurate and efficient algorithm for Bader charge integration. J.
- 654 Chem. Phys. **134**, 064111-064119 (2011).
- 655 47 Steinmann, S. N., Michel, C., Schwiedernoch, R. & Sautet, P. Impacts of electrode potentials
- and solvents on the electroreduction of CO₂: a comparison of theoretical approaches. Phys. Chem.
- 657 Chem. Phys. 17, 13949-13963 (2015).
- 658 48 Chalk, S. J. The IUPAC Gold Book website (2019).
- Humphrey, W., Dalke, A. & Schulten, K. VMD: visual molecular dynamics. J. Mol. Graph.
- 660 **14**, 33-38 (1996).
- 50 Lu, T. Molclus program. Beijing Kein Research Center for Natural Science, China (2016).
- Becke, A. D. Becke's three parameter hybrid method using the LYP correlation functional. J.
- 663 Chem. Phys. **98**, 5648-5652 (1993).
- 52 Tirado-Rives, J. & Jorgensen, W. L. Performance of B3LYP density functional methods for
- a large set of organic molecules. J. Chem. Theory Comput. 4, 297-306 (2008).
- 53 Schäfer, A., Huber, C. & Ahlrichs, R. Fully optimized contracted Gaussian basis sets of triple
- zeta valence quality for atoms Li to Kr. J. Chem. Phys. **100**, 5829-5835 (1994).
- 54 Frisch, M. et al. Gaussian 16 revision a. 03. 2016; gaussian inc. Wallingford CT. 2 (2016)
- 669 55 Grimme, S., Ehrlich, S. & Goerigk, L. Effect of the damping function in dispersion corrected
- density functional theory. J. Comput. Chem. **32**, 1456-1465 (2011).
- 671 56 Lu, T. & Chen, F. Multiwfn: a multifunctional wavefunction analyzer. J. Comput. Chem. 33,
- 672 580-592 (2012).

673

674 Acknowledgements

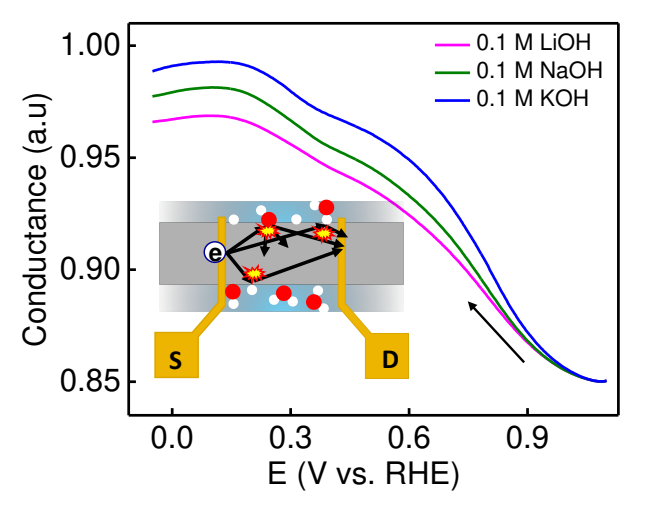
- 675 X.D. acknowledges support from the National Science Foundation award 1800580. Y.H.
- acknowledges the gracious support by NewHydrogen, Inc. Theoretical research was supported by
- the DOE-BES DE-SC0019152 grant to ANA. An award of computer time was provided by
- NERSC, and the Innovative and Novel Computational Impact on Theory and Experiment
- 679 (INCITE) program. This research used resources of the Argonne Leadership Computing Facility,
- which is a DOE Office of Science User Facility supported under Contract DE-AC02-06CH11357.

- Author contributions: XD conceived the research. The experiments were carried out by AHS
- with assistance from ZH, SW, GZ, CW under the supervision of YH and XD; and the calculations
- 683 were carried out by ZZ under the supervision of AA. The manuscript was written by AHS, ZZ,
- 684 AA, YH and XD.
- 685 **Competing interests:** The authors declare no competing interests.
- 686
- 687 Figure captions
- Fig. 1| Voltammetric studies in alkali electrolyte with different alkali metal cations. (a) CV
- (inset shows zoomed-in view of the normalized H_{upd} peak) on stationary electrode at scan rate of
- 690 100 mV/sec. (b) IR-corrected HER polarization curves collected at room temperature on
- polycrystalline Pt disc electrode in N₂-saturated 0.1 M MOH (M= Li⁺, Na⁺ and K⁺) at a scan rate of
- 5 mV/sec with rotation speed of 1600 rpm.
- Fig. 2| Schematic illustration and working principle of the ETS measurements. (a) On-chip
- PtNW device for ETS measurements [RE, CE and PtNWs (WE) are reference, counter and Pt
- 695 nanowires working electrodes respectively, S and D represents source and drain respectively]
- and (b) electrons scattering mechanism of various adsorbate molecules on PtNWs. (c) Typical
- 697 cyclic voltammogram (black), negative sweeping branch to the HER region (red) and the ETS
- spectra (blue). The red curve is divided by 10 due to much larger HER current in the HER potential
- 699 window. The OH_{des}, EDL, H_{upd} and HER regions are highlighted with different background color
- 700 (d) Normalized ETS conductance signal versus potential of PtNWs device in 0.1 M MOH
- 701 electrolyte solutions with different AM⁺.
- 702 Fig. 3| Effect of cations on adsorption of OH_{ad} at Pt(111)-water interface. (a) Adsorption
- 703 energy of OH in presence of Li⁺, Na⁺, and K⁺ ions, from static calculation and from AIMD
- simulation (statistical spread omitted here for clarity see Supplementary information). The dotted
- horizontal line marks the adsorption energy in absence of any cation. (b) The potential-dependent
- 706 G_{ad} in presence of Li⁺, Na⁺, and K⁺ ions in the potential window of 1.0 V to -1.0 V vs. RHE. (c)
- 707 Bar plot showing the dipole moment of OH_{ad} based on Bader charges. The electron density
- difference map of Pt(111)-OH_{ad}-water interface after introducing (d) Li⁺, (e) Na⁺, and (f) K⁺, plotted
- at the isovalue of 0.0025 electrons/Å³. Yellow and cyan isosurfaces represents spatial regions
- 710 experiencing increase or decrease of electron density, respectively. The insets in (d-f) are
- zoomed-in views of the OH_{ad} regions, with key isosurfaces and Bader charges on O labeled.

- Fig. 4| EIS and DFT investigation of role of adsorbed hydroxides. (a) Double layer capacitance (C_{dl}) on Pt disc electrode at different applied potentials in 0.1 M MOH solutions (M= Li⁺, Na⁺ and K⁺) (b) The radial distribution function $g_{Pt-O}(r)$ between Pt and O atoms in the Pt(111)-OH_{ad}-water interface in presence of Li⁺, Na⁺, and K⁺ ions calculated from AIMD trajectory. (c) The root mean square deviation of the position of Li⁺, with and without OH_{ad} on the Pt surface, during the 100 ps AIMD simulation. (d) Charge transfer resistance (R_{ct}) on Pt disc electrode at different applied potentials in 0.1 M MOH solutions (M= Li⁺, Na⁺ and K⁺).
- 719 Fig. 5| AIMD and micro-solvation simulation of cation and OH_{ad}. The radial distribution function g_{O-H}(r) between O and H atoms in the Pt(111)-OH_{ad}-water interface in presence of Li⁺ 720 721 in (a) covalent O-H region and (b) non-covalent O...H H-bond region. The decomposed curves 722 belong to water molecules in the hydration sphere of Li⁺, in the bulk water, or near the surface 723 OH_{ad} as its H-bond donor or acceptor. Inset in (a) shows zoomed-in view of the tail region 724 corresponding to O-H stretching. (c) Integrated $g_{O-H}(r)$ showing the coordination number (CN) of O by H at different r(O-H) distances, with dotted and dash-dot lines marking CN=2 and CN=4, 725 respectively. (d) Schematics showing the promotion of alkaline Volmer step by surface OH_{ad} at 726 the Pt(111)-water interface. (e) Optimized geometry of H₂O and Li(H₂O)₄⁺ in isolated state (top 727 728 row) or in solvated state (bottom row). (f) Bar chart of the Mayer bond order of O-H in H₂O and 729 $Li(H_2O)_4^+$ in isolated state or in solvated state.

730

Graphical Abstract



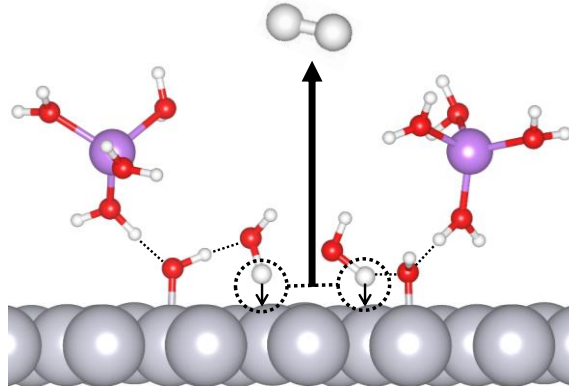


Figure 1

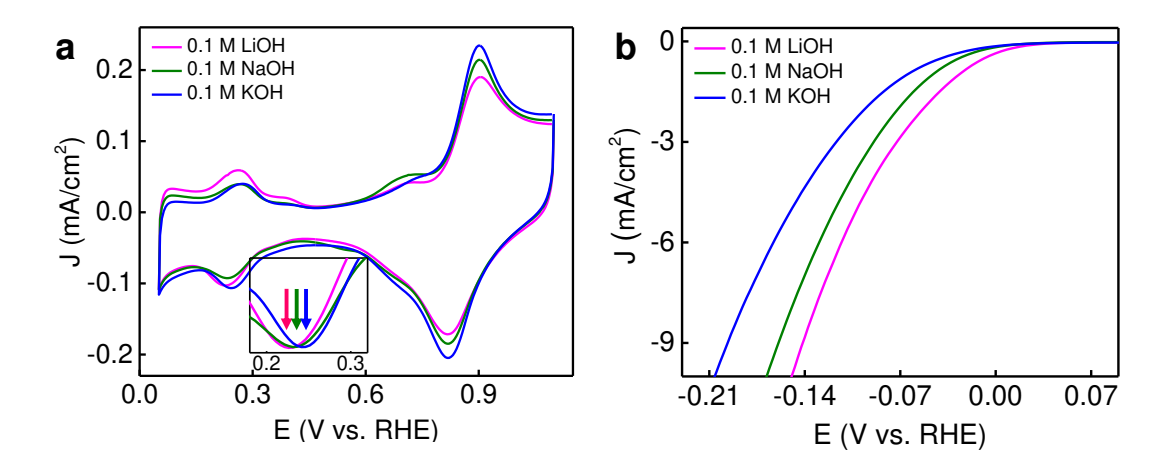


Figure 2

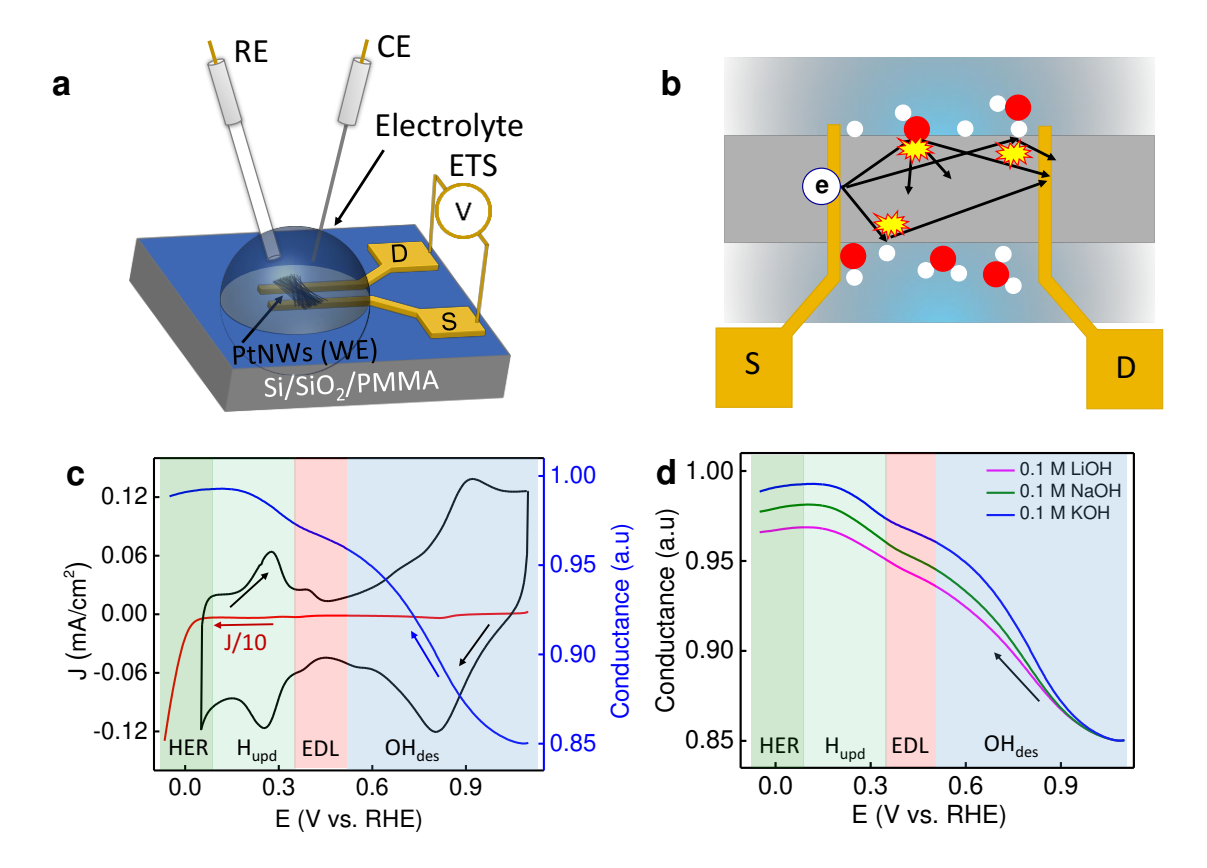


Figure 3

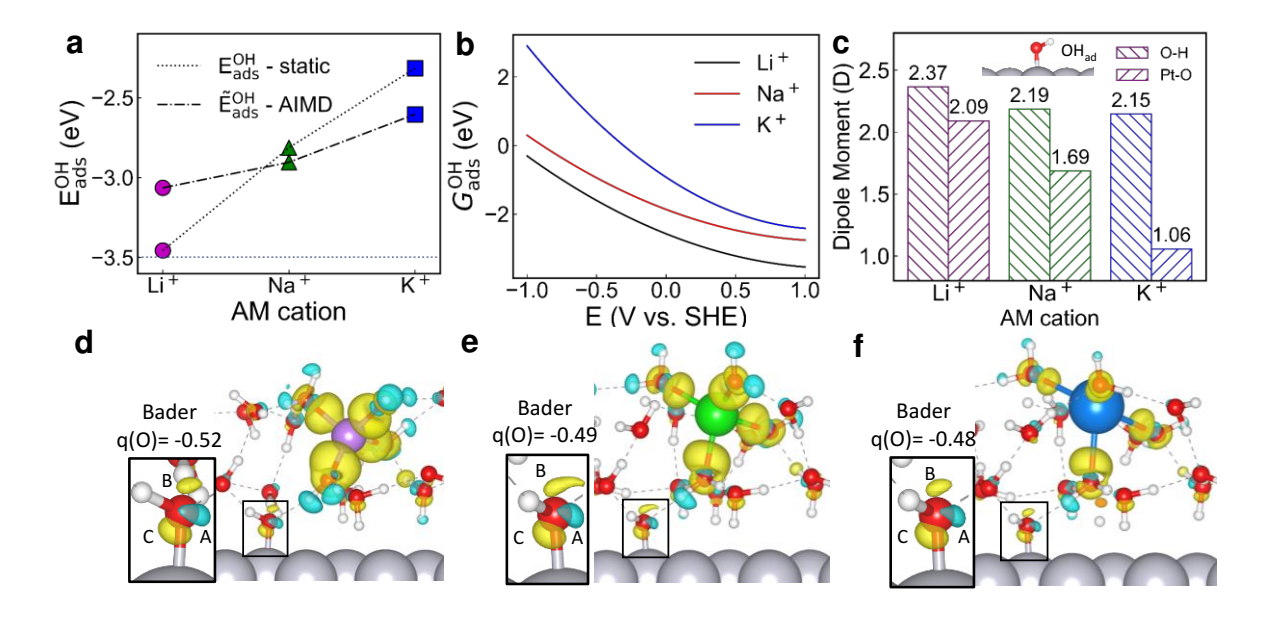


Figure 4

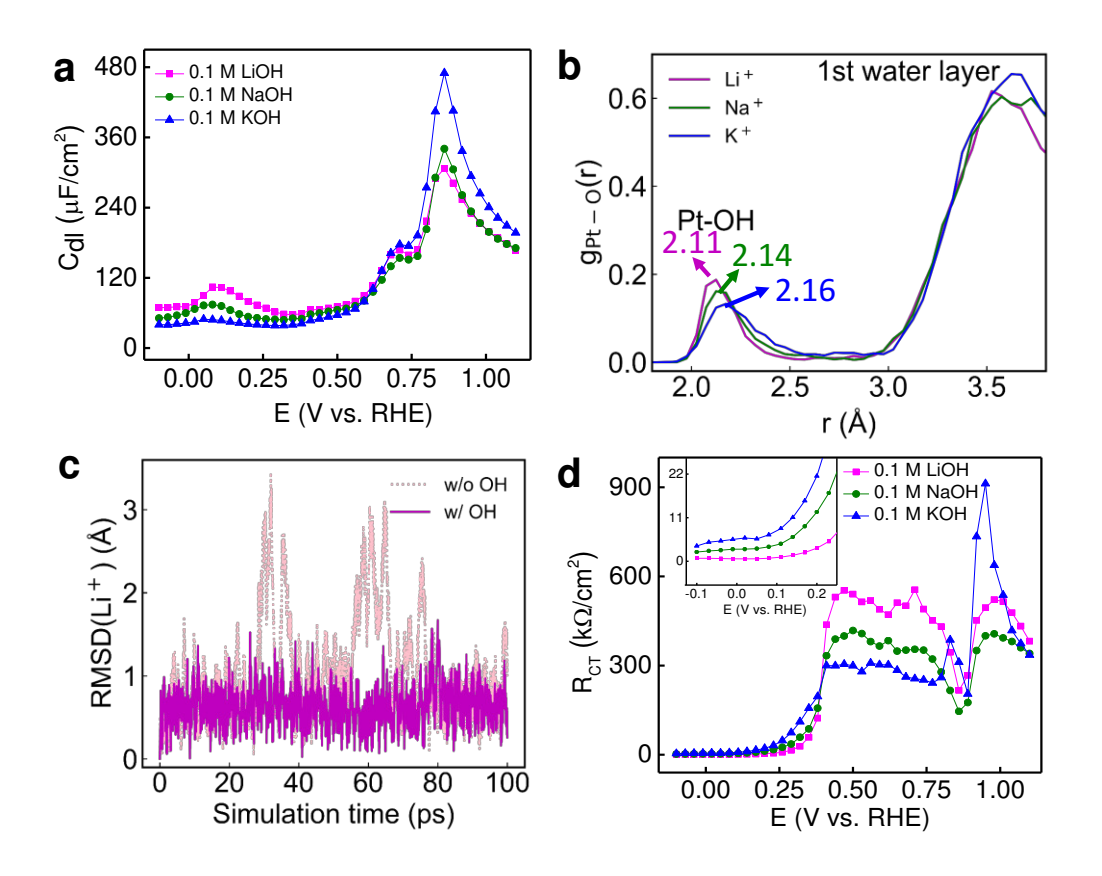


Figure 5

